AGU PUBLICATIONS

JGR

Journal of Geophysical Research: Space Physics

RESEARCH ARTICLE

10.1002/2016JA023515

Dependence of the neutron monitor count rate and time delay distribution on the rigidity spectrum of primary cosmic rays

P.-S. Mangeard[1,2,3], D. Ruffolo[1], A. Sáiz[1], W. Nuntiyakul[1,4], J. W. Bieber[3], J. Clem[3], P. Evenson[3], R. Pyle[3], M. L. Duldig[5], and J. E. Humble[5]

[1]Department of Physics, Faculty of Science, Mahidol University, Bangkok, Thailand, [2]National Astronomical Research Institute of Thailand, Chiang Mai, Thailand, [3]Bartol Research Institute and Department of Physics and Astronomy, University of Delaware, Newark, Delaware, USA, [4]Faculty of Science, Chandrakasem Rajabhat University, Bangkok, Thailand, [5]School of Physical Sciences, University of Tasmania, Hobart, Tasmania, Australia

Key Points:
- For neutron monitor latitude surveys in 2000–2007 we analyzed the count rate and the leader fraction *L* from neutron time delay histograms
- We compared observations with Monte Carlo simulations of cosmic ray showers, including new yield functions for a sea-level neutron monitor
- The comparison confirms that observed changes in *L* reflect cosmic ray spectral variation with changing geomagnetic cutoff and sunspot cycle

Correspondence to:
D. Ruffolo,
david.ruf@mahidol.ac.th

Citation:
Mangeard, P.-S., D. Ruffolo, A. Sáiz, W. Nuntiyakul, J. W. Bieber, J. Clem, P. Evenson, R. Pyle, M. L. Duldig, and J. E. Humble (2016), Dependence of the neutron monitor count rate and time delay distribution on the rigidity spectrum of primary cosmic rays, *J. Geophys. Res. Space Physics*, *121*, 11,620–11,636, doi:10.1002/2016JA023515.

Received 24 SEP 2016
Accepted 16 NOV 2016
Accepted article online 22 NOV 2016
Published online 20 DEC 2016

Abstract Neutron monitors are the premier instruments for precisely tracking time variations in the Galactic cosmic ray flux at GeV-range energies above the geomagnetic cutoff at the location of measurement. Recently, a new capability has been developed to record and analyze the neutron time delay distribution (related to neutron multiplicity) to infer variations in the cosmic ray spectrum as well. In particular, from time delay histograms we can determine the leader fraction *L*, defined as the fraction of neutrons that did not follow a previous neutron detection in the same tube from the same atmospheric secondary particle. Using data taken during 2000–2007 by a shipborne neutron monitor latitude survey, we observe a strong dependence of the count rate and *L* on the geomagnetic cutoff. We have modeled this dependence using Monte Carlo simulations of cosmic ray interactions in the atmosphere and in the neutron monitor. We present new yield functions for the count rate of a neutron monitor at sea level. The simulation results show a variation of *L* with geomagnetic cutoff as observed by the latitude survey, confirming that these changes in *L* can be attributed to changes in the cosmic ray spectrum arriving at Earth's atmosphere. We also observe a variation in *L* with time at a fixed cutoff, which reflects the evolution of the cosmic ray spectrum with the sunspot cycle, known as solar modulation.

1. Introduction

Neutron monitors (NMs) are ground-based detectors of secondary neutrons and other particles produced in atmospheric cascades from primary cosmic ray ions. NMs are sensitive to secondary particles that undergo nuclear interaction with a dense lead producer, inducing tertiary neutrons that are detected by proportional counters filled with BF_3 or ^{3}He gas. The count rate is the most widely used measurement from the NMs. Monitoring the count rate provides information about variations of the cosmic ray flux entering at the top of the atmosphere. Long-term variations (with the 11 year sunspot cycle and the 22 year solar magnetic cycle) and short-term variations (with the rotation period of the Sun or Earth and temporary Forbush decreases due to solar activity) have been intensively studied since the middle of the twentieth century with a worldwide NM network. The altitude and the geographic location of the detector affect the atmospheric structure and the geomagnetic field encountered by the primary particles. Combining the data from the different NMs requires a reliable characterization of the relationship, called the yield function, between the energy spectrum of the cosmic rays at the top of the atmosphere and the observed count rate. Data analysis as well as Monte Carlo simulations have often been used to provide estimates of the neutron monitor response function [*Clem and Dorman*, 2000; *Caballero-Lopez and Moraal*, 2012; *Mishev et al.*, 2013; *Nuntiyakul et al.*, 2014; *Maurin et al.*, 2015].

From 1994 to 2007, a shipborne neutron monitor with three BP-28 ($^{10}BF_3$) counter tubes which we call the mobile monitor (MM) was carried across a large range of geomagnetic cutoff rigidities to directly measure the response function and provided fruitful observations about the primary Galactic cosmic ray (GCR) spectrum [*Nuntiyakul et al.*, 2014]. Starting in 2000, thanks to special electronics, in addition to the count rate measurement, the MM was able to record histograms of the time delay between two consecutive counts in the same tube [*Bieber et al.*, 2004]. Such data are related to the multiplicity (number of counts per secondary particle) but provide additional information about variations in the cosmic ray spectrum [*Ruffolo et al.*, 2016]. So far, only a small portion of the latitude survey time delay data have been analyzed. From the multiple latitude

surveys, we now perform an analysis of the time delay histograms for varying geomagnetic cutoff rigidity by extracting a parameter introduced by *Ruffolo et al.* [2016], the leader fraction L, i.e., the fraction of counts that are not temporally associated with a previous count in the same neutron counter tube.

Section 2 presents analysis and results from the time delay histograms recorded during the latitude surveys of 2001–2007. In section 3, we detail a complete set of Monte Carlo simulations performed to model the count rate and the leader fraction L observed in the latitude survey data at varying cutoff rigidity. The comparison of observations with Monte Carlo results is discussed in sections 3.2 and 4.

2. Analysis of the Latitude Survey Data

The purpose of a latitude survey with a cosmic ray detector is to take data over a large range of cutoff rigidity in a short period of time. For each survey epoch, the derivative of the count rate as a function of cutoff rigidity, called the differential response function, is the NM yield function times the cosmic ray spectrum. Although the three-tube MM had a smaller size than most fixed NMs, there are clear advantages of using such an instrument to study the cosmic ray spectrum as opposed to using multiple fixed NM stations: (i) the single detector system requires no intercalibration; (ii) the geomagnetic field can be used as a continuous spectrometer; and (iii) a wide range of rigidity cutoffs can be covered, up to more than 16 GV. The only modern fixed station at such high cutoff, the Princess Sirindhorn Neutron Monitor station located in Thailand at a vertical cutoff of ~16.8 GV, began operating afterward, in August 2007.

The MM and its operation were described by *Nuntiyakul et al.* [2014], and so they are discussed only briefly in this article. The MM was composed of three proportional counter tubes of standard NM64 design [*Hatton and Carmichael*, 1964], in other words a 3NM64. The MM was installed inside an insulated container (called the TasVan) carried by one of the Polar Class icebreakers of the U.S. Coast Guard. As shown in Figure 1, a typical journey of the ship through the Pacific Ocean started from Seattle (USA) in November. The ship traveled to McMurdo Base in Antarctica during the austral summer and returned to Seattle in April. In the following, the "survey year" refers to the year in which the survey began.

2.1. Time Delay Distributions

For each of the three tubes, the electronics provided hourly time delay histograms with different time scales as presented in Figure 2. For more details about the experimental determination of the histograms, we refer to *Ruffolo et al.* [2016]; in particular, the present measurements used the 600 series electronics described there. The long time histogram presents an exponential tail representing the coincidence time delay distribution between two uncorrelated incoming secondary particles (SPs, mostly neutrons). The short time histogram, which is actually a zoom in the long time histogram, shows the nonexponential excess at short time delays that can be attributed to the time delays between neutrons produced in the same secondary particle interaction in the lead.

It has been shown by *Ruffolo et al.* [2016] that it is possible to extract a parameter from the time delay histograms, the leader fraction L, which is the statistically determined fraction of neutron counts that did not follow a related count due to the same primary cosmic ray. The L value is the inverse of the average multiplicity, i.e., the average number of counts produced by a secondary particle. Three methods can be used to estimate L from the time delays histograms [see *Ruffolo et al.*, 2016, section 3.1]. In the present work, we use the first method, in which L is determined by

$$L = \frac{1 - e^{-\alpha t_0}}{\alpha e^{\alpha t_d}} A \tag{1}$$

where α and A are the parameters from the long time histogram fitted to the function $\tilde{n}(t) = Ae^{-\alpha t}$, $t_0 = 142$ ms is the overflow time in the electronic system, and $t_d \sim 80$–90 μs is the electronic dead time in the circuit dedicated to the computation of the time delay histograms.

2.2. Data Selection

The full available data set was first cleaned using the redundancy of the three tubes and anomalous time periods were excluded as described in section 3 of *Nuntiyakul et al.* [2014]. As in that work, periods including Forbush decreases larger than 10% at the McMurdo NM were removed. In addition to this selection, we excluded from the analysis any period of time with at least one problematic neutron counter tube. The time delay distributions during survey year 2000 were recorded with an early version of the electronics. In order to

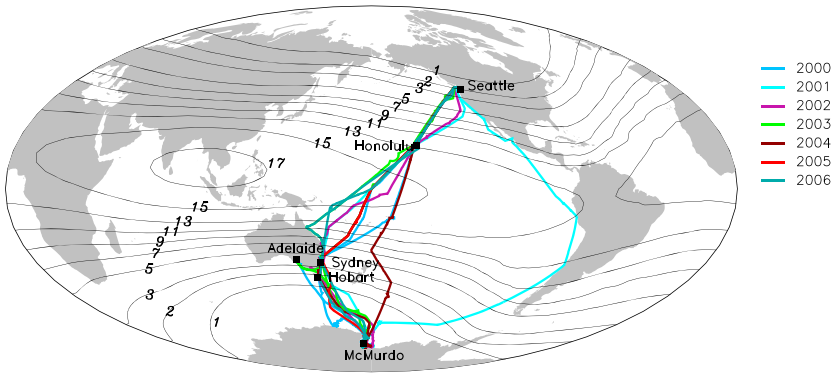

Figure 1. Tracks of the shipborne neutron monitor latitude surveys from 2000 to 2007, superimposed on contours of the vertical cutoff rigidity in GV. The year of a survey refers to the year in which it started.

avoid systematic effects from the firmware version, those data have also been excluded in the present analysis. Thus, only six surveys starting from 2001 have been used here.

The method described above requires sufficient statistics to properly fit a histogram and thus to extract the leader fraction from the time delay distribution. Due to the low count rate per tube at sea level, typically between 4 and 13 Hz, the histograms have been summed for every 3 h. We assume here that during a period of 3 h, the count rate as well as the rigidity cutoff are relatively constant. Then, for a given 3 h period at time t, the total leader fraction is computed as

$$L(t) = \sum_{i=1}^{3} f_i(t) L_i(t) \tag{2}$$

where $L_i(t)$ is the leader fraction of the ith tube as calculated from the time delay distribution and $f_i(t)$ is the contribution fraction of the ith tube to the total number of recorded time delays for the period t. Due to its central position in the 3NM64 configuration, the contribution of the middle tube, f_2, is larger than the individual contributions of the two edge tubes. Typical values were $f_1 \sim 0.32$, $f_2 \sim 0.36$, and $f_3 \sim 0.32$. Note that with this definition, L for the whole detector assesses the same information as each individual L_i, i.e., the ratio of the total number of leader counts by the total number of counts for the whole detector.

The geomagnetic rigidity cutoff R_c used in this analysis is the apparent cutoff presented by *Clem et al.* [1997], using the efficient calculation technique presented by *Bieber et al.* [1997]. For every location and time of data operations, nine incoming directions (the vertical one and eight directions with a zenith angle of 30°) are used to determine R_c. Thus, the anisotropy of the geomagnetic field and the east-west asymmetry at low latitude are taken into account.

2.3. Observational Results

For each of the six surveys, L is sorted per bin of R_c. Figure 3 presents the results. Each point shows the mean value of L for the corresponding bin, and the error bar corresponds to the standard error. For each survey year,

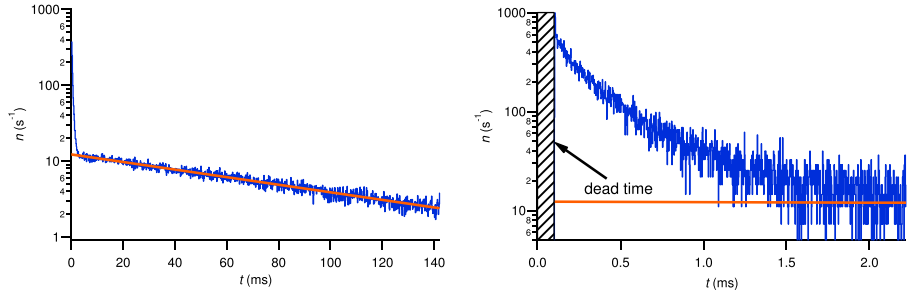

Figure 2. Distribution of the time delay between successive neutron counts at one counter tube recorded during one specific 3 h interval. (left) Long time delays show the exponential distribution typical of unrelated events, while (right) short time delays deviate substantially from the exponential function (red line). The electronic dead time is typically $t_d \sim 80 - 90\,\mu s$.

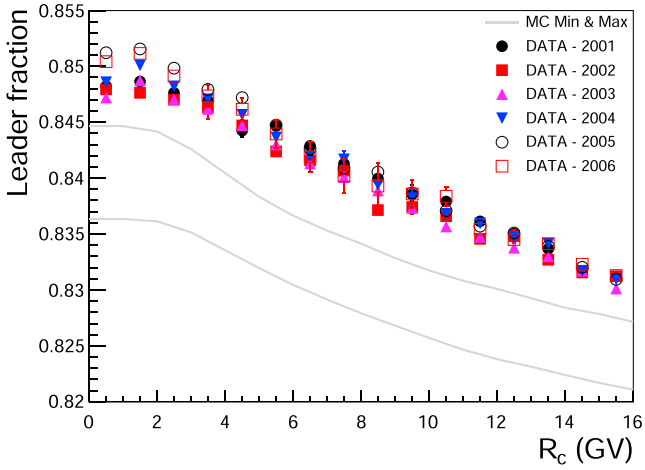

Figure 3. Dependence of the leader fraction L measured by the mobile neutron monitor on the apparent cutoff rigidity R_c for the six surveys operating with the same firmware, together with the range of Monte Carlo results for various cosmic ray spectra and atmospheric profiles. This confirms that the observed L is related to the rigidity spectrum of primary cosmic rays impinging on Earth's atmosphere. Note the overall dependence on time at a given R_c, which is clearest at low R_c, reflecting the variation of the cosmic ray spectrum with the sunspot cycle, known as solar modulation. Monte Carlo results reproduce those trends but slightly underestimate the absolute value of L.

a decrease from ~0.85 to ~0.83 is clearly visible when R_c increases within the available range. This observation confirms that L is related to the cosmic ray spectrum. The dependence of L on R_c is explained by the increased relative contribution of highly energetic primary particles (PPs) to the count rate at higher cutoff. A higher PP energy leads to a higher energy of the induced SPs and hence a higher multiplicity and lower leader fraction. Figure 3 also contains results from Monte Carlo simulations that will be discussed later in this paper.

The modulation due to changes in solar activity also impacts the value of L, as found by *Ruffolo et al.* [2016] for a fixed station. At low R_c, a variation up to ~0.004 is observed between the different surveys with a larger L for survey years 2005 and 2006, which correspond to a period of low solar activity, weaker solar modulation, and softer GCR spectra. Due to the lower modulation amplitude of the GCRs at high rigidity, this effect is smaller and cannot be clearly observed at high cutoff rigidity with the available data set.

The systematic decrease of L from the R_c range of 1 to 2 GV to the range of 0 to 1 GV could be related to a significant decrease of the atmospheric pressure near Antarctica, which is the location where the survey reached $R_c < 1$ GV. It is standard for NM count rates to be corrected for the effect of atmospheric pressure variations, which would otherwise dominate over cosmic ray flux variations. Similarly, the leader fraction at Doi Inthanon, Thailand, is corrected for a positive correlation with pressure variations [*Ruffolo et al.*, 2016]. However, in each case the pressure effect needs to be determined from a large data set with good statistics. In the present work, the statistics for L are insufficient to determine the pressure effect, so L has not been corrected for pressure variation. We can merely speculate that there could be a positive correlation between L and atmospheric pressure, as found at Doi Inthanon, because as the atmospheric depth seen by the primary particles is lower, the SP spectra are harder, and L decreases. This could account for the lower L value for R_c of 0 to 1 GV.

3. Monte Carlo Simulations

3.1. Methods

We performed Monte Carlo simulations using the software FLUKA 2011 [*Ferrari et al.*, 2005; *Bohlen et al.*, 2014] with the interaction model DPMJET-II.5 as recommended in the FLUKA manual. In this work we use the method presented in *Mangeard et al.* [2016], consisting of three stages: (i) interactions due to primary cosmic rays in the Earth's atmosphere are simulated and secondary particle fluxes are extracted at the altitude of the detector plus six meters, (ii) the sensitivity of the detector (including its surroundings) is determined for nine species of SPs, and (iii) both simulation outputs are combined to estimate the detector response to primary cosmic rays as well as the leader fraction.

3.1.1. Primary Cosmic Ray Spectrum

The simulated primary particles are protons (up to 1000 GeV) and alphas (up to 2000 GeV). Their distributions are assumed to be isotropic at the top of the Earth's atmosphere. Simulations are performed for different ranges of kinetic energies with the flux assumed to be uniform over kinetic energy within each range; the desired spectrum is implemented later by means of weighting. The transport through the atmosphere is determined without a geomagnetic field. Every SP produced by interactions in the atmosphere is linked to its PP. The SPs are selected postsimulation depending on the rigidity cutoff at the location of the detector.

Table 1. Characteristics of the Five Atmospheric Profiles

Name of Profile	McM	Hob	Sea4	Sea11	Hon
Location	McMurdo	Hobart	Seattle	Seattle	Honolulu
Latitude (deg)	77.86S	42.88S	47.59N	47.59N	21.3N
Longitude (deg)	166.65E	147.34E	122.34W	122.34W	157.87W
Period	Jan–Feb	Dec	Apr	Nov	Nov
R_c (GV)	0.1	1.71	1.73	1.73	12.6
Pressure P (mmHg)	745.3	756.8	760.4	763.8	761.5
Atmosphere depth D (g cm^{-2})	1013.0	1031.4	1035.8	1040.5	1039.8

The cosmic ray spectrum above the atmosphere is modeled postsimulation using weights according to the chosen model and solar activity. There is a systematic uncertainty from the choice of the local interstellar spectrum (LIS) of GCR protons. While the *Voyager 1* spacecraft has traveled beyond the heliopause, and its data [*Stone et al.*, 2013] can provide improved observational constraints on the LIS [*Bisschoff and Potgieter*, 2016; *Ghelfi et al.*, 2016], there are differing opinions as to whether Voyager 1 is directly measuring the LIS [e.g., *Scherer et al.*, 2011; *Zhang et al.*, 2015], and in this sense the LIS remains somewhat uncertain. To estimate the effect of the uncertain LIS, we employed a variety of LIS models for which the model dependence of the modulation parameter has been investigated by *Herbst et al.* [2010]. Effects from the GCR heliospheric modulation are determined with the widely used force field approximation of *Gleeson and Axford* [1968]. Despite some limitations exposed by *Caballero-Lopez and Moraal* [2004], the force field approximation allows a relatively good parameterization of the modulation with only one parameter (ϕ). This simplicity allows us to easily discuss the variations of the detector response with respect to the solar activity. The expression of the fluxes and of the modulation depends on the differentiating energy variable: the kinetic energy per nucleon T or the rigidity R. In the rest of this paper, this variable is indicated via a subscript. Let $\mathrm{LIS}_{T,i}$ be the LIS in terms of T, i.e., $\mathrm{d}N_i/\mathrm{d}T$, where N_i refers to the number of PP of type i (proton or alpha) per unit area, unit time, and unit solid angle at the edge of the heliosphere. The primary cosmic ray spectrum above the Earth's atmosphere can be expressed as a function of T and ϕ:

$$G_{T,i}(T,\phi) = \mathrm{LIS}_{T,i}(T+\Phi_i)\frac{T(T+2E_r)}{(T+\Phi_i)(T+\Phi_i+2E_r)}, \tag{3}$$

where $E_r = 938$ MeV/nucleon, $\Phi_i = (eZ_i/A_i)\phi$, and Z_i and A_i are the charge and the atomic number of the PP, respectively. If we express the flux in terms of R, the modulation relation becomes a function of R and ϕ:

$$G_{R,i}(R,\phi) = \frac{R^2}{(R+\phi)^2}\mathrm{LIS}_{R,i}(R+\phi). \tag{4}$$

Note here that ϕ can vary from a few hundred to more than a thousand MV during a solar cycle. As discussed by *Herbst et al.* [2010], the value of the modulation parameter ϕ actually depends significantly on the chosen LIS. *Herbst et al.* [2010] also determined linear relations between the modulation parameters for four different LISs with respect to the parameter ϕ_{US05} determined by *Usoskin et al.* [2005]. We use those relations for the parameter ϕ_{US11} (an updated version of ϕ_{US05} by *Usoskin et al.* [2011]). In this way, we tested five different LISs, each with an appropriate time-dependent modulation parameter derived from ϕ_{US11}. During the period of interest, ϕ_{US11} varied roughly from 350 to 1000 MV, so those two values are used in the simulation as boundaries for the solar activity during the latitude survey period (the peak $\phi_{\mathrm{US11}} > 1200$ MV in November 2003 occurred in the recovery period from a large Forbush decrease of 28 October 2003, which is removed from this analysis). In addition to those models, direct measurements of the proton and alpha spectra from the Payload for Antimatter Matter Exploration and Light-nuclei Astrophysics (PAMELA) satellite are also used. The proton spectrum combined data measured for the period of 13 November to 4 December 2006 [*Adriani et al.*, 2013] up to a break energy $E_{k,b} \sim 48.62$ GeV, and data from the period 2006–2008 [*Adriani et al.*, 2011] at higher energy, assuming a negligible solar modulation above $E_{k,b}$. We lowered the latter spectrum by 3.2% according to the footnote of *Adriani et al.* [2013]. The He spectrum comes only from the measurements of *Adriani et al.* [2011].

A significant fraction of the NM count rate is due to cosmic nuclei heavier than He impinging on the top of the atmosphere. Their contribution is simulated by applying the appropriate factor F_{hn} to the flux of alphas.

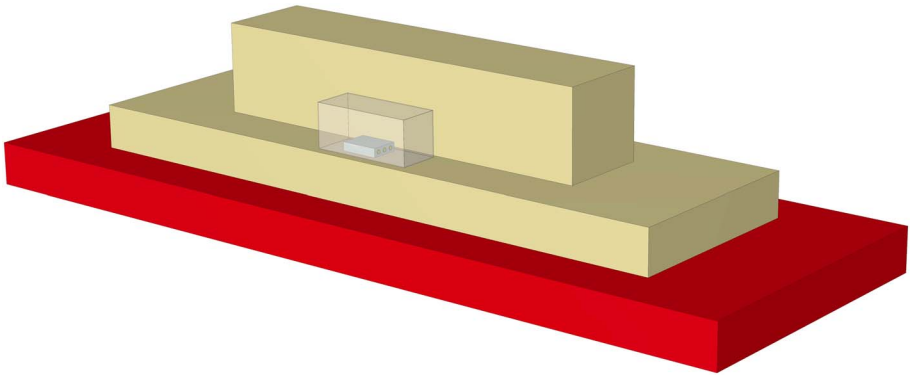

Figure 4. Model geometry for Monte Carlo simulation of the mobile neutron monitor in a shipping container on board a ship.

In the case of the LIS models, expressed in terms of kinetic energy per nucleon in *Herbst et al.* [2010], the overall ratio of nucleons in nuclei with $Z \geq 2$ (modeled as α particles) to protons is set to 0.3 following *Usoskin et al.* [2011]. In the case of the spectra from PAMELA for which the flux of alphas is measured, nuclei heavier than alphas at a given kinetic energy per nucleon are assumed to contribute a fraction $F = 0.354$ of the nucleons from cosmic rays heavier than protons, so we multiplied the PAMELA He spectrum in terms of kinetic energy per nucleon by the factor $F_{hn} = 1/(1 - F) = 1.548$ [*Caballero-Lopez and Moraal*, 2012].

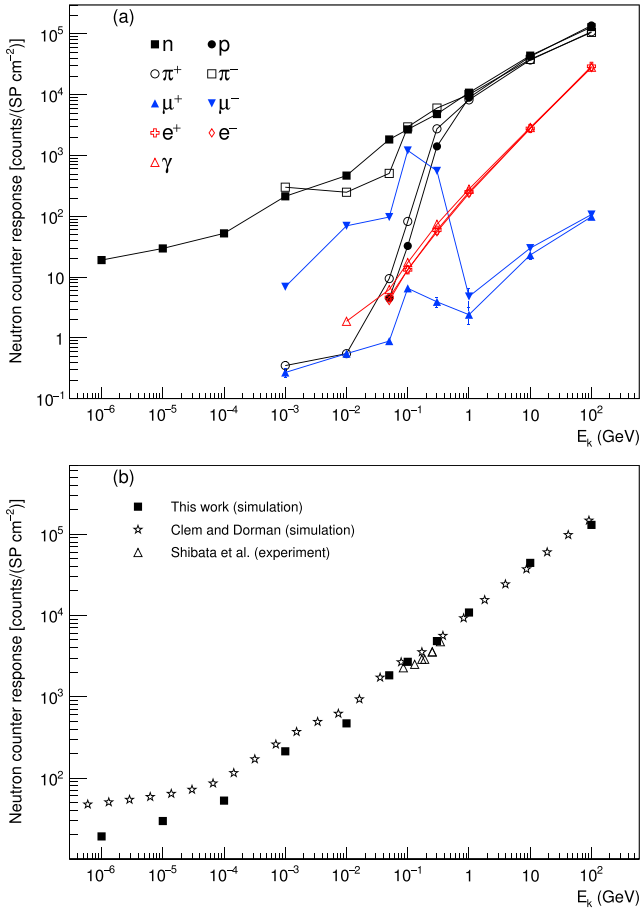

Figure 5. (a) Simulated response of the middle neutron counter tube as function of the secondary particle (SP) kinetic energy for various SP species at vertical incidence. (b) Comparison of the simulated neutron counter response to secondary neutrons from the present work and from *Clem and Dorman* [2000] along with experimental data from *Shibata et al.* [1997, 1999].

Table 2. Percentage Contributions of Various Cosmic Ray Shower Components to the MM Count Rates in Monte Carlo Simulations

Secondary Particle	Contribution (%)
$n, E_k < 10$ MeV	1.74(1)
n, 10 MeV $\leq E_k < 1$ GeV	79.6(5)
$n, E_k \geq 1$ GeV	8.1(1)
p	5.93(8)
μ^-	3.01(2)
μ^+	0.614(3)
γ	0.563(3)
e^-	0.153(1)
e^+	0.144(1)
π^-	0.128(8)
π^+	0.088(6)

3.1.2. Atmospheric Model

The atmospheric models we use represent typical profiles in temperature, pressure, and composition of the air with respect to altitude at the location of interest. The detailed calculation of the profiles used in this work is explained in the appendix of *Mangeard et al.* [2016]. The profiles combine information from the Global Data Assimilation System (https://ready.arl.noaa.gov/gdas1.php) at altitude up to ~26 km and the Naval Research Laboratory Mass Spectrometer, Incoherent Scatter Radar Extended model (NRLMSISE-00) [*Picone et al.*, 2002] at higher altitude. The simulation of the cascade development stops at an altitude of 6 m above the altitude of the detector. In the FLUKA simulation, the first 6 m over the detector are modeled by a fully absorbant (*blackhole*) material. Particles entering this layer are recorded as SPs along with their characteristics and those of their parent PP. Simulations of the cosmic ray interactions in the air were performed separately for five atmospheric models according to the typical journey of the ship: Seattle (Sea11) and Honolulu (Hon) in November, Hobart (Hob) in December, McMurdo (McM) in January and February, and Seattle (Sea4) in April. Their main characteristics are presented in Table 1. For each simulation, about 48 million (SP, PP) pairs were recorded.

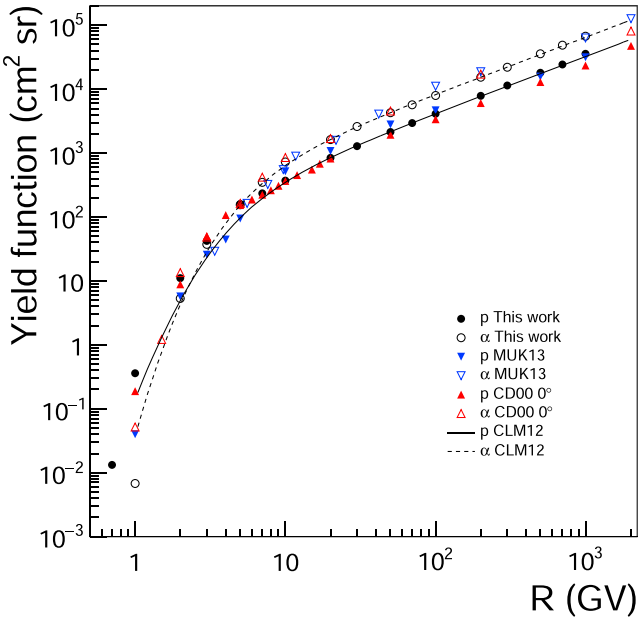

Figure 6. Simulated yield functions of the MM for primary cosmic ray p and α using the Sea4 atmospheric profile (P =760.4 mmHg and D =1035.8 g cm^{-2}) from the present work and previous results (scaled to three neutron counters) from *Mishev et al.* [2013] (MUK13) and from *Clem and Dorman* [2000] (CD00; vertical incidence only). The empirical yield functions from *Caballero-Lopez and Moraal* [2012] are presented for comparison.

Table 3. Proton Yield Functions of a Standard 3NM64 at Sea Level for Various Electronic Dead Times

		Counts Per Primary Flux (cm^2 sr)				
		Dead Time				
R (GV)	E_k/Nucleon (GeV)	0 s	20 μs	100 μs	1.2 ms	4 ms
0.5	0.1249	—	—	—	—	—
0.7	0.2324	1.34*e*−2	1.33*e*−2	1.30*e*−2	1.19*e*−2	1.18*e*−2
1	0.4331	3.65*e*−1	3.62*e*−1	3.52*e*−1	3.20*e*−1	3.18*e*−1
2	1.271	1.12*e*+1	1.10*e*+1	1.07*e*+1	9.60*e*+0	9.51*e*+0
3	2.205	4.26*e*+1	4.21*e*+1	4.06*e*+1	3.61*e*+1	3.57*e*+1
5	4.149	1.61*e*+2	1.59*e*+2	1.52*e*+2	1.33*e*+2	1.31*e*+2
7	6.125	2.38*e*+2	2.34*e*+2	2.24*e*+2	1.94*e*+2	1.91*e*+2
10	9.106	3.78*e*+2	3.72*e*+2	3.54*e*+2	3.05*e*+2	3.01*e*+2
20	19.08	8.59*e*+2	8.43*e*+2	7.99*e*+2	6.81*e*+2	6.71*e*+2
30	29.08	1.31*e*+3	1.28*e*+3	1.21*e*+3	1.03*e*+3	1.01*e*+3
50	49.07	2.18*e*+3	2.14*e*+3	2.01*e*+3	1.70*e*+3	1.67*e*+3
70	69.07	3.04*e*+3	2.97*e*+3	2.79*e*+3	2.34*e*+3	2.30*e*+3
100	99.07	4.23*e*+3	4.13*e*+3	3.87*e*+3	3.24*e*+3	3.19*e*+3
200	199.1	8.06*e*+3	7.83*e*+3	7.30*e*+3	6.06*e*+3	5.95*e*+3
300	299.1	1.18*e*+4	1.14*e*+4	1.06*e*+4	8.76*e*+3	8.59*e*+3
500	499.1	1.86*e*+4	1.80*e*+4	1.67*e*+4	1.38*e*+4	1.35*e*+4
700	699.1	2.53*e*+4	2.44*e*+4	2.26*e*+4	1.85*e*+4	1.81*e*+4
1000	999.1	3.73*e*+4	3.58*e*+4	3.30*e*+4	2.68*e*+4	2.62*e*+4

3.1.3. MM Response to Secondary Particles

The response of the MM to the SPs was estimated with a separate simulation. The geometry of the surroundings has been included inside the FLUKA geometry editor. The ship has been simulated as three hollow boxes (three decks) of stainless steel (thickness of 2 cm) as well as the shipping container as a smaller hollow box (thickness of 2.54 cm) as presented in Figure 4. The geometry reflects the actual placement of the shipping container on an upper deck to the side of the superstructure. The air composition is defined as that in the first layer of the atmospheric simulation, and the pressure chosen is the one from the McMurdo profile. As shown by *Clem and Dorman* [2000], the contribution of nonvertical SPs must be taken into account in the Monte Carlo simulation. Moreover, the position of the detector on board and the structure of the ship is not invariant with the incident azimuthal angle of the secondary particle. Following the method from *Mangeard et al.* [2016], many sets of simulations have been performed depending on the type of particle, the kinetic energy, and the incident direction with five zenith angles θ (0°, 15°, 30°, 50°, and 70°) and eight azimuthal angles φ (from 0° to 315°). The beam is centered and located at 6 m over the MM with a rectangular area of 100 m^2 for vertical incidence. The area is expanded depending on the incidence angle in order for the beam to cover the detector well [*Aiemsa-ad et al.*, 2015]. An electronic dead time of 28.4 μs has been used for the middle tube and 19.4 μs for the edge tubes, according to the experimentally determined dead times.

The determination of the leader fraction from the simulation results is simpler than the determination from the data for three reasons: (i) the absence of chance coincidences, (ii) the capability to identify each count with a specific simulated secondary particle, and (iii) the knowledge of the time of the boron disintegration. The dead time of the time delay electronics (known for each tube thanks to the time delay histograms) is then imposed. As reported in *Ruffolo et al.* [2016], the dead time in the time delay electronics is about ~62 μs larger than the dead time in the count rate electronics. A value of 90.4 μs is used for the middle tube and 81.4 μs for the edge tubes. The leader fraction is then determined as the ratio of the number of SPs giving at least one count to the total number of counts.

3.2. Monte Carlo Results

3.2.1. Count Rate as Related to Secondary Particles

Figure 5a presents the number of boron disintegrations (counts) in the middle counter tube of the 3NM64 per beam luminosity (SP cm^{-2}), i.e., the counter response, for beams of vertically incident SPs of various types. The response generally increases with increasing energy. Above 1 GeV, the detection efficiencies of hadronic,

Table 4. Alpha Particle Yield Functions of a Standard 3NM64 at Sea Level for Various Electronic Dead Times

		Counts Per Primary Flux (cm^2 sr)				
		Dead Time				
R (GV)	E_k/nucleon (GeV)	0 s	20 μs	100 μs	1.2 ms	4 ms
0.5	0.0327	—	—	—	—	—
0.7	0.0632	—	—	—	—	—
1	0.1249	6.80*e*−3	6.75*e*−3	6.59*e*−3	6.09*e*−3	6.05*e*−3
2	0.4331	5.37*e*+0	5.32*e*+0	5.17*e*+0	4.69*e*+0	4.65*e*+0
3	0.8311	3.76*e*+1	3.72*e*+1	3.60*e*+1	3.22*e*+1	3.19*e*+1
5	1.732	1.57*e*+2	1.56*e*+2	1.50*e*+2	1.32*e*+2	1.31*e*+2
7	2.685	3.54*e*+2	3.49*e*+2	3.35*e*+2	2.94*e*+2	2.90*e*+2
10	4.149	7.39*e*+2	7.29*e*+2	6.96*e*+2	6.04*e*+2	5.96*e*+2
20	9.106	1.66*e*+3	1.64*e*+3	1.56*e*+3	1.34*e*+3	1.32*e*+3
30	14.09	2.64*e*+3	2.59*e*+3	2.46*e*+3	2.10*e*+3	2.07*e*+3
50	24.08	4.35*e*+3	4.26*e*+3	4.04*e*+3	3.43*e*+3	3.38*e*+3
70	34.07	5.78*e*+3	5.67*e*+3	5.36*e*+3	4.55*e*+3	4.47*e*+3
100	49.07	8.15*e*+3	7.98*e*+3	7.52*e*+3	6.35*e*+3	6.25*e*+3
200	99.07	1.57*e*+4	1.53*e*+4	1.44*e*+4	1.21*e*+4	1.18*e*+4
300	149.1	2.28*e*+4	2.22*e*+4	2.08*e*+4	1.73*e*+4	1.70*e*+4
500	249.1	3.70*e*+4	3.59*e*+4	3.35*e*+4	2.78*e*+4	2.73*e*+4
700	349.1	5.03*e*+4	4.88*e*+4	4.54*e*+4	3.76*e*+4	3.68*e*+4
1000	499.1	7.01*e*+4	6.78*e*+4	6.29*e*+4	5.18*e*+4	5.07*e*+4

electromagnetic and muonic SPs are clearly separated. The hadronic SPs are the most efficient in producing counts. The response to protons and π^+ drops strongly below ~200 MeV, but the response to neutrons and π^- remains strong due to the greater possibility of binding with and disrupting a lead nucleus to produce neutrons that result in counts. The response to electromagnetic SPs increases by about 4 orders of magnitude from 10–100 MeV to 100 GeV but remains significantly lower than that of hadronic SPs. Note that the photonuclear resonance in the lead (~10–15 MeV) is not present in the plot and the simple line between 10 MeV and 50 MeV is not a proper estimation of the response to photons in the resonant energy range. We estimate that neglecting this resonance in the present work affects the count rate by ~1%. The response to μ^+ is about 3 orders of magnitude lower than that for neutrons. Above 1 GeV, the efficiency of μ^- is similar to that for μ^+, but below this energy, μ^- are much more efficient in producing counts. Due to its negative charge and small Bohr radius, a μ^- is likely to be bound to and absorbed by a lead nucleus that then deexcites by emitting neutrons that can enhance the count rate.

The contributions of the nine species of SPs to the total count rate are presented in Table 2. Percentages were determined using the atmosphere model "Sea4" at sea level for the case of PAMELA spectra and no geomagnetic cutoff. About 89.4% of the counts are produced by neutrons, mostly between 10 MeV and 1 GeV. However, about 10% of the count rate is due to the other SPs. Protons make the second largest contribution, 6%. Muons at sea level mostly have an energy between 1 and 100 GeV, where the detection efficiency is very low, so their contribution to the count rate remains low, ~3.6% (mostly μ^- with E_k<10 GeV). The electromagnetic component of the atmospheric shower at sea level is mainly at energies lower than 1 GeV, where the detector sensitivity is very low. Thus, the contributions of γ and $e^{\pm}$ to the count rate are minor. Despite the high sensitivity of the detector to pions, those SPs provide only a minor contribution to the total count rate due to their low fluxes at sea level. This is why the detector is called a *neutron monitor*.

We compared our simulation results with previous FLUKA work by *Clem and Dorman* [2000] and with experimental determination of efficiency of the NM64 by *Shibata et al.* [1997, 1999] (Figure 5b). The experimental results were obtained using neutron beams impacting about half of a 1NM64 detector. This includes more reflector than in our simulation of a 3NM64. All results were normalized to a 3NM64 middle tube response using the coefficients from *Mangeard et al.* [2016]. We observe a good agreement between the two simulations above 50 MeV where most of the counts come from. Differences at lower energy may be explained by different geometries and surroundings implemented in the simulations, and environmental details have

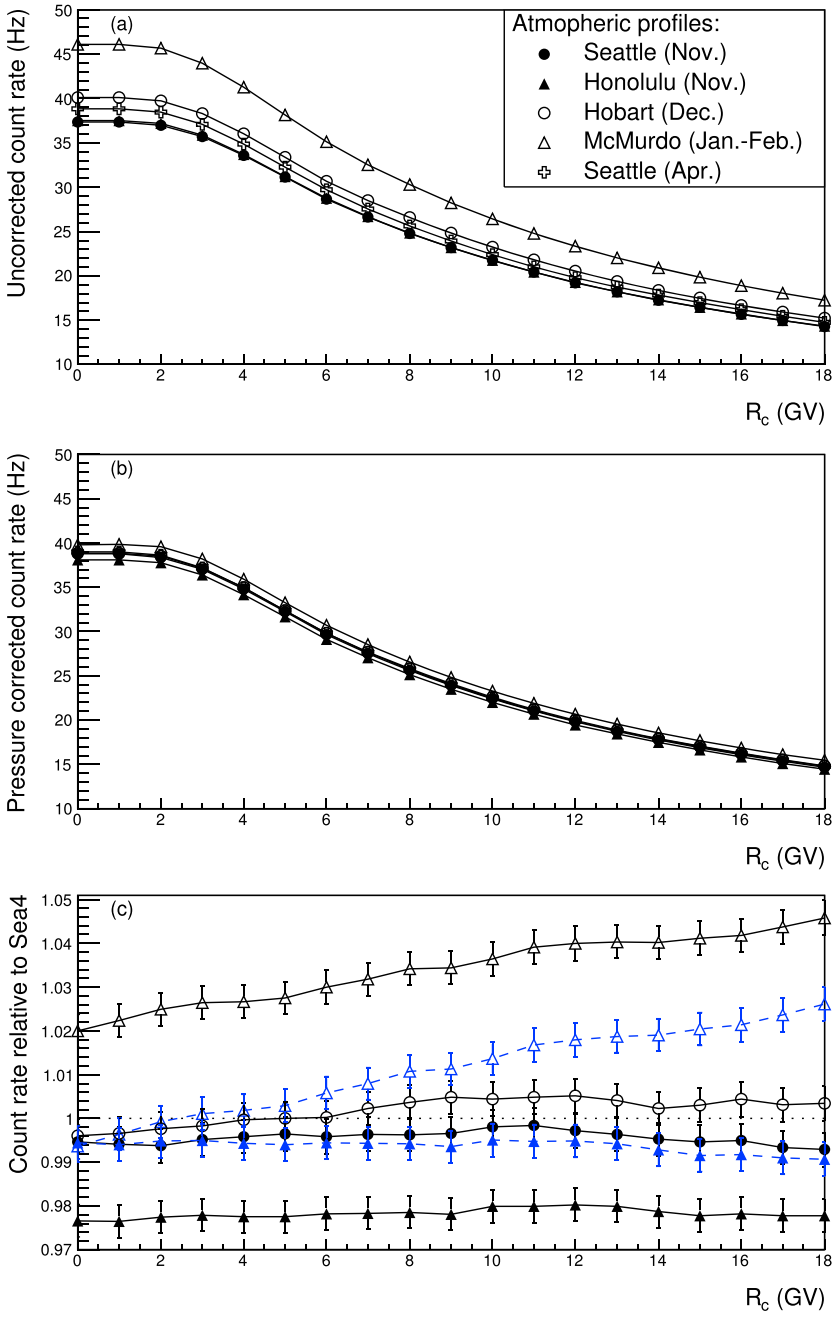

Figure 7. Dependence of the simulated count rate on the apparent cutoff rigidity R_c for the five atmospheric profiles. (a) Count rate as uncorrected for pressure. (b) Count rate corrected for pressure. (c) Black: Pressure corrected count rate relative to that for Seattle in April. Dashed blue: Relative count rate corrected using the effective pressure, for McM and Hon, which brings the relative count rates closer to unity.

significant effects on the neutron spectrum at this range of energy. Note, however, that such neutrons have little effect on the count rate (see Table 2). For this comparison, a dead time of 20 μs was used in all cases. To estimate the experimental response in terms of counts (SP $cm^{-2})^{-1}$, we multiplied the efficiency values from *Shibata et al.* [1997, 1999] by the area of a 1NM64 (48.5 × 226.5 cm^2). To take into account the difference between a 1NM64 counter tube and the middle tube of the simulated 3NM64, we multiplied the experimental 1NM64 efficiencies by a factor of 1.46 [*Shibata et al.*, 2001], because an additional ~46% of that

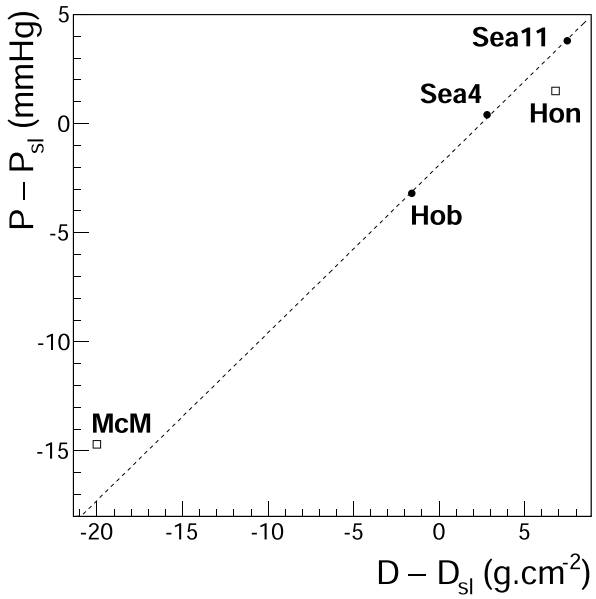

Figure 8. Deviation of the pressure P from the mean sea level pressure P_{sl} with respect to the deviation of the atmospheric depth D from the mean sea level atmospheric depth D_{sl} for the five atmospheric profiles. The relation for the profiles Hob, Sea4, and Sea11 (dots) can be fitted by a straight line of equation $y(x) = 0.77x - 1.9$ (dashed line). The points for the profiles McM and Hon (open squares) lie significantly away from the straight line. The fitted function is used to estimate effective pressures for McM and Hon.

count rate is expected in a middle tube due to neutrons impinging at the lead around neighboring tubes. Considering the differences in setup and uncertainties, the experimental results and simulations are in fairly good agreement.

3.2.2. Count Rate as Related to Primary Cosmic Rays

Our simulated yield functions for the profile Sea4 (760.4 mmHg; 1035.8 g cm^{-2}), calculated using monoenergetic and isotropic fluxes of protons and alphas, are presented by circles in Figure 6. The yield functions are expressed in counts per primary particle per cm^2 sr. The yield function values for protons and alphas are presented in Tables 3 and 4, respectively. Figure 6 also shows previous Monte Carlo simulation results for sea level by *Clem and Dorman* [2000] (vertical incidence only) and *Mishev et al.* [2013], as well as empirical yield functions that aim to explain latitude survey data by *Caballero-Lopez and Moraal* [2012]. We have corrected a printing error in the first five values of the alpha yield function in Table 1 of *Mishev et al.* [2013] (I. Usoskin, private communication, 2016). The previous Monte Carlo results were scaled from 6NM64 to 3NM64 configurations using the simulated normalization coefficients from *Mangeard et al.* [2016]. An electronic dead time of 20 μs is assumed. At high rigidity, the various yield functions are similar and the yield function for alphas is higher than that for protons by a factor of ∼2, roughly corresponding to the ratio of the total kinetic energy of an alpha and a proton at the same rigidity. In our results, the crossover at low rigidity between alpha and proton yield functions occurs at ∼5 GV, which is ∼3 GV higher than the value determined by *Clem and Dorman* [2000] and that reported in Figure 4 of *Caballero-Lopez and Moraal* [2012] and is compatible with the crossover of *Mishev et al.* [2013]. The proton yield function in our results below 100 GV is mostly similar to that of *Clem and Dorman* [2000] but seems to be significantly overestimated below 7 GV in comparison with *Caballero-Lopez and Moraal* [2012].

The systematic effect of the choice of the atmospheric profile as a function of the rigidity cutoff is shown in Figure 7, using PAMELA spectra of primary cosmic rays. Here and in other figures the error bars on Monte Carlo results indicate the statistical uncertainty. As expected the absolute difference of the count rate between the five profiles (Figure 7a) is dominated by the barometric effect. The simulated count rates were corrected to a mean sea level pressure P_{sl} =760 mmHg using

$$C_P = Ce^{\beta(P-P_{sl})}, \quad (5)$$

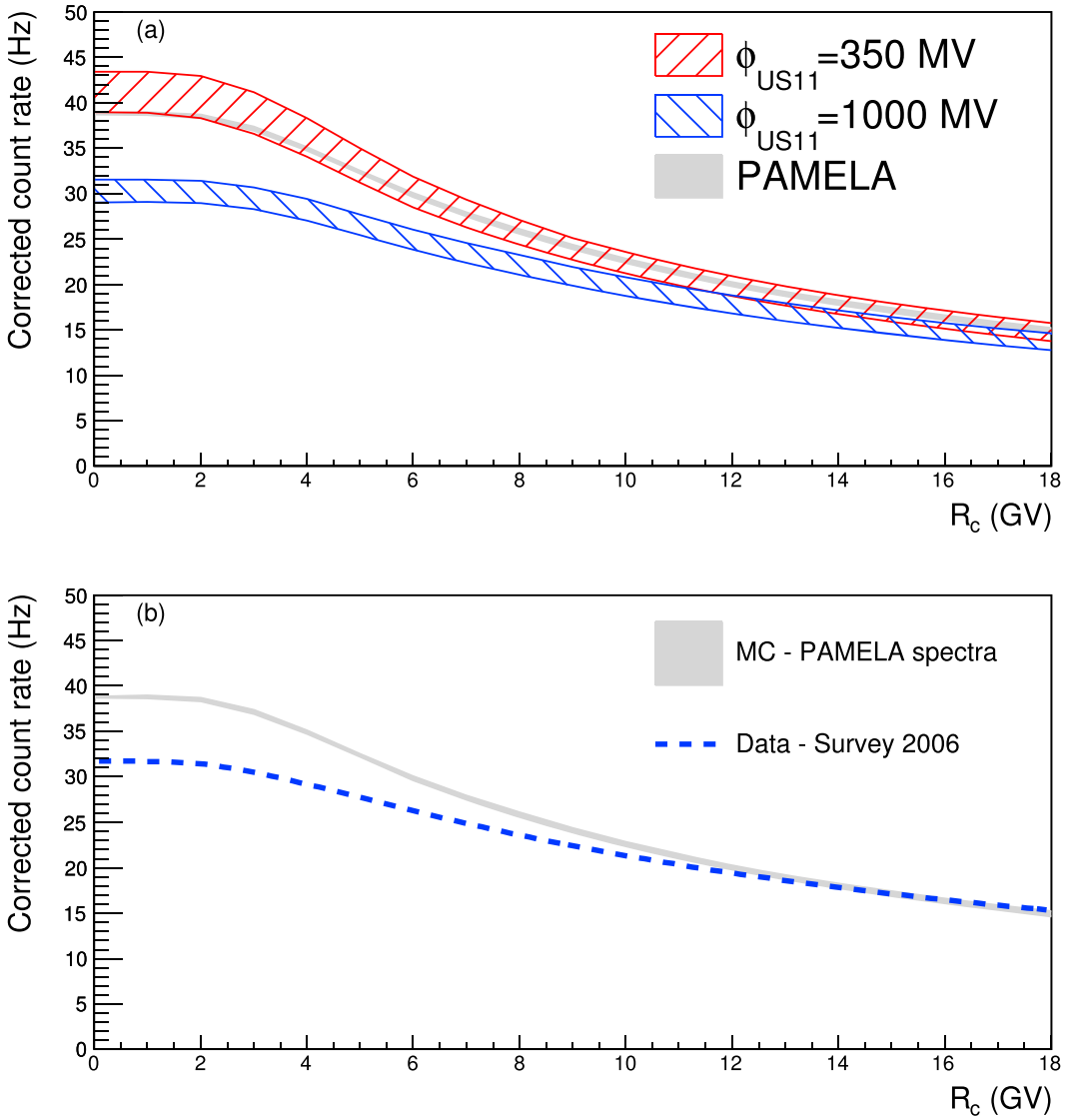

Figure 9. Dependence of the simulated pressure corrected count rates on the apparent cutoff rigidity R_c. (a) Several assumptions of local interstellar spectrum are presented, from *Herbst et al.* [2010], for two values of the solar modulation parameter ϕ_{US11} that bracket the range of values during the latitude survey period. The PAMELA spectra used here, for 2006, correspond to solar modulation at about 400 MV. (b) Comparison between the simulated response function for PAMELA spectra with the Dorman function from the 2006 latitude survey [*Nuntiyakul et al.*, 2014]. There is a substantial discrepancy from the data at $R_c \lesssim 6$ GV.

where P is the pressure, C the count rate, and C_P the count rate corrected for pressure variation. The pressure correction coefficient β, in units of percent per mmHg, was empirically determined by *Nuntiyakul et al.* [2014] and depends on the cutoff rigidity R_c (in GV):

$$\beta = 1.006 - 0.01534 R_c. \tag{6}$$

In other words, in order to correct the count rate, the variation of pressure is used here as a proxy of the variation of the atmospheric depth D with respect to a mean sea level atmospheric depth D_{sl} =1033 g cm^{-2}. The agreement between the two profiles at Seattle and the one at Hobart is ∼1% (Figure 7b). This shows the quality of the empirical correction for pressures close to P_{sl} and relatively similar profiles. For the other two profiles ("McM" and "Hon"), a remaining shift of ± ∼1 Hz can be observed after the pressure correction. Looking at McMurdo at $R_c = 0$ GV and at Honolulu at high R_c, i.e., in the real geomagnetic conditions, Figure 7c

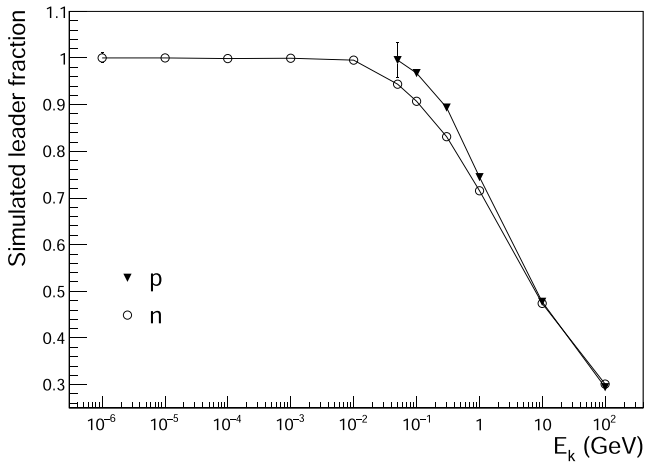

Figure 10. Simulated leader fraction of the middle neutron counter tube as a function of secondary proton or neutron kinetic energy at vertical incidence.

indicates that the pressure correction procedure of *Nuntiyakul et al.* [2014] can be expected to achieve the correction within about ±2%.

Much of the remaining difference of McM and Hon profiles relative to Sea4 is explained by the nonlinearity of the relation between the variation of P around P_{sl} and the variation of D around D_{sl} for the five simulated profiles. As one can see in Figure 8, the linearity holds well for the three profiles where the pressure correction gives good results ("Hob", Sea4, and "Sea11"). For McM and Hon, which are very different in terms of latitude, humidity, temperature, and vertical atmospheric structure, a different correction must be applied. In order to apply an appropriate correction, we determined, for each of those two profiles, an effective pressure P_{eff} such that

$$P_{eff} - P_{sl} = y\left(D - D_{sl}\right) \tag{7}$$

where $y(\Delta D)$ is the function of the straight line of Figure 8. We obtained $P_{eff,McM} = 742.3$ mmHg and $P_{eff,Hon} = 763.3$ mmHg. Figure 7c shows that the agreement after the final correction is around 1%. In the

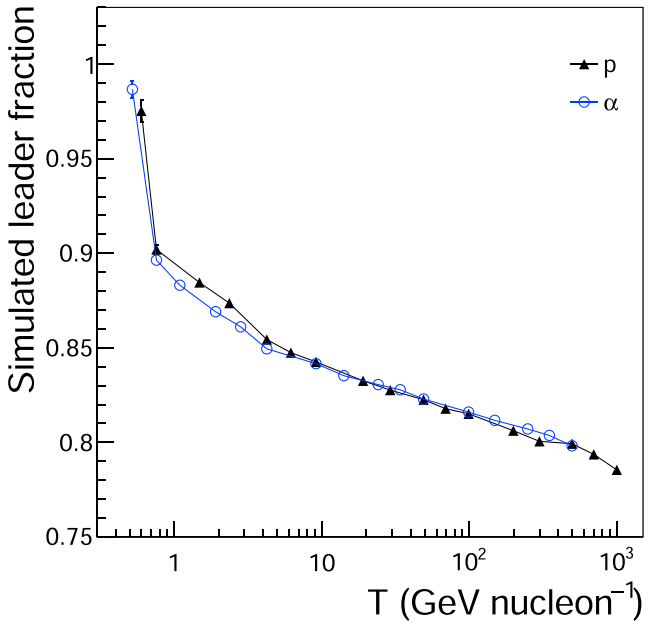

Figure 11. Simulated leader fraction for the MM as a function of kinetic energy per nucleon, T, of primary cosmic ray p and α using the atmospheric profile Sea4 ($P = 760.4$ mmHg; $D = 1035.8$ g cm^{-2}).

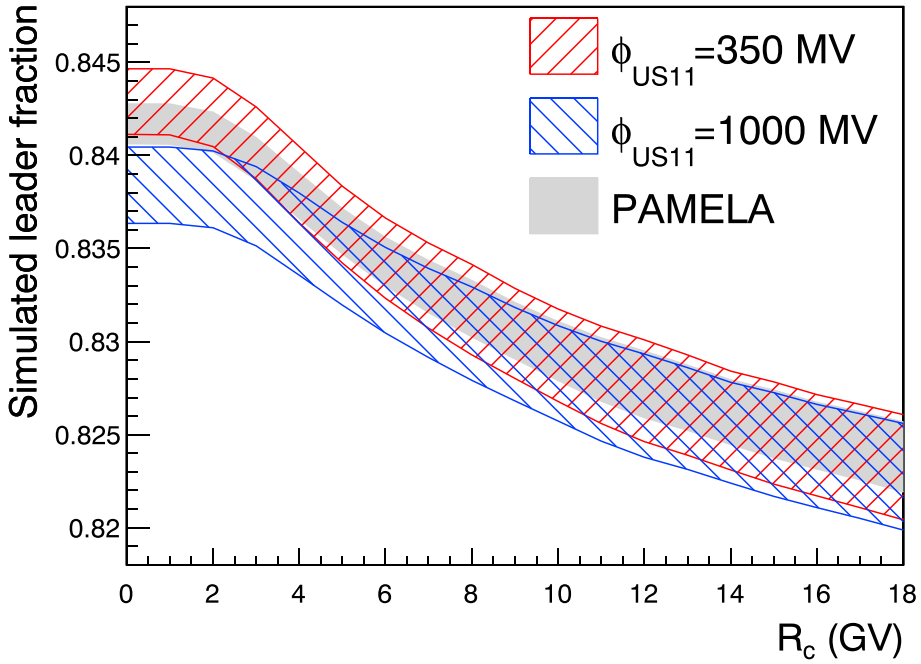

Figure 12. Monte Carlo results for the leader fraction as a function of the apparent cutoff rigidity R_c for five atmospheric profiles and five assumptions of the local interstellar spectrum from *Herbst et al.* [2010], for two values of the solar modulation intensity that bracket the range of values of ϕ_{US11} during the latitude survey period. In addition, we show the range of Monte Carlo results based on PAMELA spectra for 2006 corresponding to a solar modulation of about 400 MV.

case of McM, where the pressure is significantly different ($|P_{McM} - P_{sl}| \sim 15$ mmHg), the difference from Sea4 progressively increases to a level of 2–3% for $R_c > 12$ GV. This indicates that the correction is not sufficient at high-rigidity cutoff and at low atmospheric pressure. The lack of data with a large $|P - P_{sl}|$ at a location with a large R_c [see *Nuntiyakul*, 2014, Appendix B] probably contributes to this remaining shift.

The effects from the choice of LIS model were estimated. As we can see in Figure 9a, there are systematic variations due to the choice of model and more generally to the chosen primary cosmic ray spectrum. While the pressure effect is small and relatively constant with R_c, this LIS effect depends strongly on R_c as

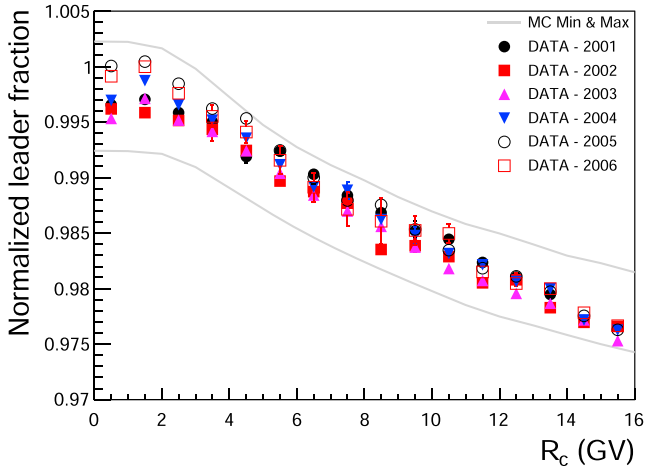

Figure 13. Dependence of the leader fraction L measured by the mobile neutron monitor on the apparent cutoff rigidity R_c for the six surveys operating with the same firmware, together with the range of Monte Carlo results for various cosmic ray spectra and atmospheric profiles. Observations were normalized relative to the leader fraction for the 1–2 GV cutoff rigidity bin for survey year 2006 (0.851). Simulation results are normalized to the calculated leader fraction at R_c =1 GV using PAMELA spectra and the Sea11 atmosphere (0.843).

well as on the solar modulation. This finding is in agreement with previous work, which shows variations from 10 to 30% between different computed count rates [*Clem and Dorman*, 2000] and between different LIS models [*Herbst et al.*, 2010]. Taking into account the nonvertical primary particles at the top of the atmosphere does not reduce the yield function at low rigidities, and the simulated differential response function is still largely overestimated under 10 GV (Figure 9b) in comparison with latitude survey data. Finally, the difference of response to primary cosmic rays between the middle tube and the edge tubes is noticeable in our simulated results where the edge-to-middle tube count rate ratio decreases from about 0.894 at $R_c = 0$ GV to 0.892 at $R_c = 16$ GV, for PAMELA spectra.

3.2.3. Leader Fraction as Related to Secondary Particles

Figure 10 presents the variation of the leader fraction in the middle tube with kinetic energy for SP protons and neutrons with vertical incidence angle, using the measured dead time of 90.4 μs for time delay data; note that the dead time for the count rate is much shorter at 28.4 μs. As expected, the more energetic hadronic SPs undergo interactions (typically in the producer) with greater multiplicity (lower L). The leader fraction for hadronic SPs is highly dependent on the SP energy and decreases from $L \approx 1$ at 1 MeV to $L < 0.5$ at 10 GeV. Neutrons with energy lower than 1 MeV typically produce at most only one count; the corresponding leader fraction is consequently about 1. As was found for the count rate, the asymmetric surroundings have significant effects on L, depending on the incidence angle. For instance, in the middle tube for a beam of 100 MeV neutrons, the azimuthal dependence (∼1%) of the leader fraction at nonzero zenith angle is associated with the ship's structure due to attenuation of the high-energy portion of the neutron beam along with production of less energetic neutrons as the beam passes though the metal structure. The same effect, upon passage through the atmosphere, explains an overall increase in L at high zenith angle.

3.2.4. Leader Fraction as Related to Primary Cosmic Rays

The leader fraction has been also calculated using monoenergetic and isotropic fluxes of primary cosmic ray protons and alphas. Figure 11 shows a decrease of L with the kinetic energy per nucleon of the simulated primary particle. Above 10 GeV, protons and alphas of the same energy per nucleon give the same L value. It can be interpreted that the secondary particle spectrum (at sea level) is similar for both types of primaries for the same energy per nucleon.

The leader fraction, L_{MC}, was determined from simulation results as a function of the cutoff rigidity for realistic models of the primary cosmic ray spectrum. For each of two solar modulation parameters, $\phi_{US11} = 350$ and 1000 MV, which bracket the range of values during the latitude surveys, Figure 12 shows the ranges of L_{MC} values for the 25 combinations of 5 LIS + force field models and the 5 atmospheric profiles. The range of results using PAMELA spectra for five atmospheric profiles is also shown. Note that no pressure correction is applied to the leader fraction. L_{MC} decreases by ∼0.02 as the apparent rigidity cutoff increases from 0 to 18 GV. The solar modulation is stronger at low rigidity, where the ranges of L_{MC} values for $\phi_{US11} = 350$ and 1000 MV are separated. At large R_c, for a given ϕ_{US11} deviations between results for different LIS models and for atmospheric profiles are larger than at low R_c. The overlap of the bands shows that the variation with the solar modulation is smaller at large R_c. Figures 3 and 13 show that the Monte Carlo results can explain the observed changes in L, both with respect to the cutoff rigidity R_c and with respect to the solar modulation, with a nearly constant shift in the absolute value. This confirms that changes in L can be used as an indicator of the spectral variation of the primary cosmic ray flux at the top of the atmosphere.

4. Discussion

In this work, we further explore the use of the leader fraction L determined from neutron monitor time delay histograms to indicate changes in the primary cosmic ray spectrum. Our analysis of multiple latitude surveys (from 2001 to 2006) provides the first measurements of the variation of a neutron monitor leader fraction L with geomagnetic cutoff rigidity and with solar modulation. To confirm that the observed changes in L indeed indicate changes in the cosmic ray spectrum, we developed a Monte Carlo simulation of the mobile neutron monitor. We determined the sea-level yield functions for the MM count rate as well as expected variations in the count rate and L.

Our results show an absolute count rate agreement within 22% between our Monte Carlo results and latitude survey observations from *Nuntiyakul et al.* [2014] with a better agreement, <5%, at large cutoff rigidity. Note that to account for overall changes in the MM count rate for some (but not all) surveys, presumably due to different placement and surroundings of the MM on the ship from year to year, *Nuntiyakul et al.* [2014] nor-

malized the MM count rate in those surveys based on the count rate ratio of the MM to the NM at McMurdo, Antarctica while the ship was near McMurdo, with changes up to 4.7%. This shows that the varying placement of the MM on the ship affected the observed count rate by up to 4.7%, implying an uncertainty on the Monte Carlo estimation of the count rate. In any case, our Monte Carlo results overestimate the count rate at low cutoff rigidity by more than this uncertainty.

If the count rate is normalized to 1 at $R_c = 0$ GV, the normalized count rate at a given R_c represents the fractional contribution of primary cosmic rays at $R > R_c$ to the total count rate at all P. Our simulated results predict the contribution to the count rate of the primary cosmic rays at $R_c > 17$ GV to be about 40.2%, compared with about 50.2% in the observation. Comparing to the Figure 4 of *Mishev et al.* [2013] that gathers several previous results for an equivalent solar modulation, our values are in agreement with previous results of simulation using the GEANT4 simulation package [*Agostinelli et al.*, 2003] by *Debrunner et al.* [1982], *Flückiger et al.* [2008] and *Matthiä et al.* [2009]. We obtain a better agreement with the observation than the previous FLUKA simulation results by *Clem and Dorman* [2000], which predict a much lower contribution (<35%) from primary particles with $R_c > 17$ GV. We do not achieve a relative agreement with normalized latitude survey data as good as in *Mishev et al.* [2013] and *Gil et al.* [2015], which use GEANT4 with PLANETOCOSMICS [*Desorgher et al.*, 2005]. This may be due to the change of the hadronic interaction model used by FLUKA from DPMJET at $T > 5$ GeV nucleon^{-1} to the Relativistic Quantum Molecular Dynamics (RQMD) model at lower T. The transition energy is within our energy range of interest. Improvements in the FLUKA atmospheric shower development calculation are needed to achieve a better agreement between the observed and simulated count rates for the primary particles with a rigidity lower than 10 GV. At $R_c > 12$ GV, we note that absolute (unnormalized) agreement between our simulated and observed count rates is very good (<5%).

We studied the systematic effect from the choice of atmospheric profile. The count rate can be corrected for pressure and atmospheric depth differences. After correction, the agreement between the count rates using the five atmospheric profiles is at the level of ∼1%. We studied the systematic effect of the choice of the cosmic ray spectrum at the top of the atmosphere. In particular, we employed five existing models of the local interstellar spectrum (LIS) together with the force field model for a previously tabulated solar modulation parameter as a function of time, adjusted as appropriate for each model [*Herbst et al.*, 2010]. We also used the spectrum observed by PAMELA during 2006 (for details see section 3.1.1). The difference between Monte Carlo results for different LIS models represents the dominant uncertainty in Monte Carlo estimation of both the count rate and the leader fraction.

There is a shift of about 1% in the absolute value of L between data and Monte Carlo simulation (Figure 3). This could be explained by an incomplete simulation of the detection process within the detector (e.g., all boron disintegrations are counted in the simulation). The simple geometry for simulation of the ship may also impact the SP interactions in the surroundings of the MM and modify the energy distributions of the SPs that produce counts.

The observed variations of L with changing cutoff rigidity and solar modulation are consistent with our Monte Carlo simulation results, confirming that L can be used as an indicator of cosmic ray variation.

Acknowledgments
This work was partially supported by the postdoctoral research sponsorship of Mahidol University; the Thailand Research Fund award RTA5980003; the United States National Science Foundation awards PLR-1245939, PLR-1341562, and their predecessors; and the Australian Antarctic Division. We thank the officers and crew of the USCG icebreakers Polar Star and Polar Sea for their assistance in conducting the surveys. We also thank Leonard Shulman, James Roth, and Keith Bolton for their technical assistance in preparing and maintaining the TasVan and enclosed mobile monitor; Suttiwat Madlee for visualization assistance; and Andrew Snodin for setting up and maintaining the computing cluster on which our simulations were performed. The data displayed in the figures are available upon request to the corresponding author.

References

Adriani, O., et al. (2011), PAMELA measurements of cosmic-ray proton and helium spectra, *Science*, *332*, 69–72, doi:10.1126/science.1199172.

Adriani, O., et al. (2013), Time dependence of the proton flux measured by PAMELA during the 2006 July–2009 December solar minimum, *Astrophys. J.*, *765*, 91, doi:10.1088/0004-637X/765/2/91.

Agostinelli, S., et al. (2003), Geant4—A simulation toolkit, *Nucl Instr. Meth. Phys. Res. A*, *506*, 250–303.

Aiemsa-ad, N., et al. (2015), Measurement and simulation of neutron monitor count rate dependence on surrounding structure, *J. Geophys. Res. Space Physics*, *120*, 5253–5265, doi:10.1002/2015JA021249.

Bieber, J. W., J. Clem, and P. Evenson (1997), Efficient computation of apparent cutoffs, in *25th International Cosmic Ray Conference*, vol. 2, pp. 389–392, World Scientific, Durban, South Africa.

Bieber, J. W., J. M. Clem, M. L. Duldig, P. A. Evenson, J. E. Humble, and R. Pyle (2004), Latitude survey observations of neutron monitor multiplicity, *J. Geophys. Res.*, *109*, A12106, doi:10.1029/2004JA010493.

Bisschoff, D., and M. S. Potgieter (2016), New local interstellar spectra for protons, helium and carbon derived from PAMELA and Voyager 1 observations, *Astrophys. Space Sci.*, *361*, 48, doi:10.1007/s10509-015-2633-8.

Bohlen, T. T., F. Cerutti, M. P. W. Chin, A. Fassò, A. Ferrari, P. G. Ortega, A. Mairani, P. R. Sala, G. Smirnov, and V. Vlachoudis (2014), The FLUKA code: Developments and challenges for high energy and medical applications, *Nuclear Data Sheets*, *120*, 211–214.

Caballero-Lopez, R. A., and H. Moraal (2004), Limitations of the force field equations to describe cosmic ray modulation, *J. Geophys. Res.*, *109*, A01101, doi:10.1029/2003JA010098.

Caballero-Lopez, R. A., and H. Moraal (2012), Cosmic-ray yield and response functions in the atmosphere, *J. Geophys. Res.*, *117*, A12103, doi:10.1029/2012JA011794.
Clem, J., J. W. Bieber, P. Evenson, D. Hall, J. E. Humble, and M. Dulding (1997), Contribution of obliquely incident particles to neutron monitor counting rate, *J. Geophys. Res.*, *102*, A12, doi:10.1029/97JA02366.
Clem, J., and L. Dorman (2000), Neutron monitor response functions, *Space Sci. Rev.*, *93*, 335, doi:10.1023/A:1026508915269.
Debrunner, H., E. Flückiger, and J. Lockwood (1982), Specific yield function S(P) for a neutron monitor at sea level, paper presented at 8th Europ. Cosmic Ray Symposium, Rome.
Desorgher, L., E. O. Flückiger, M. Gurtner, M. R. Moser, and R. Bütikofer (2005), Atmocosmics: A geant 4 code for computing the interaction of cosmic rays with the Earth's atmosphere, *Int. J. Modern Phys. A*, *20*, 6802–6804, doi:10.1142/S0217751X05030132.
Ferrari, A., P. R. Sala, A. Fassò, and J. Ranft (2005), FLUKA: A multi-particle transport code. CERN, Geneva, CERN-2005-10, INFN/TC_05/11, SLAC-R-773.
Flückiger, E. O., M. R. Moser, B. Pirard, R. Bütikofer, and L. Desorgher (2008), A parameterized neutron monitor yield function for space weather applications, in *30th International Cosmic Ray Conference*, vol. 1, pp. 289–292, Universidad Nacional Autónoma de México, Mexico City, Mexico.
Ghelfi, A., F. Barao, L. Derome, and D. Maurin (2016), Non-parametric determination of H and He interstellar fluxes from cosmic-ray data, *Astron. Astrophys.*, *591*, A94, doi:10.1051/0004-6361/201527852.
Gil, A., I. G. Usoskin, G. A. Kovaltsov, A. L. Mishev, C. Corti, and V. Bindi (2015), Can we properly model the neutron monitor count rate?, *J. Geophys. Res. Space Phys.*, *120*, 7172–7178, doi:10.1002/2015JA021654.
Gleeson, L. J., and W. I. Axford (1968), Solar modulation of Galactic cosmic rays, *Astrophys. J.*, *154*, 1011–1026.
Hatton, C. J., and H. Carmichael (1964), Experimental investigation of the NM-64 neutron monitor, *Can. J. Phys.*, *42*, 2443–2472.
Herbst, K., A. Kopp, B. Heber, F. Steinhilber, H. Fichtner, K. Scherer, and D. Matthiä (2010), On the importance of the local interstellar spectrum for the solar modulation parameter, *J. Geophys. Res.*, *115*, D00I20, doi:10.1029/2009JD012557.
Mangeard, P.-S., D. Ruffolo, A. Sáiz, S. Madlee, and T. Nutaro (2016), Monte Carlo simulation of the neutron monitor yield function, *J. Geophys. Res. Space Physics*, *121*, 7435–7448, doi:10.1002/2016JA022638.
Matthiä, D., B. Heber, G. Reitz, M. Meier, L. Sihver, T. Berger, and K. Herbst (2009), Temporal and spatial evolution of the solar energetic particle event on 20 January 2005 and resulting radiation doses in aviation, *J. Geophys. Res.*, *114*, A08104, doi:10.1029/2009JA014125.
Maurin, D., A. Cheminet, L. Derome, A. Ghelfi, and G. Hubert (2015), Neutron monitors and muon detectors for solar modulation studies: Interstellar flux, yield function, and assessment of critical parameters in count rate calculations, *Adv. Space Res.*, *55*, 363–389, doi:10.1016/j.asr.2014.06.021.
Mishev, A. L., I. G. Usoskin, and G. A. Kovaltsov (2013), Neutron monitor yield function: New improved computations, *J. Geophys. Res. Space Physics*, *118*, 2783–2788, doi:10.1002/jgra.50325.
Nuntiyakul, W. (2014), Analysis of data from a calibration neutron monitor at Doi Inthanon and a ship-borne neutron monitor, PhD Thesis, Mahidol Univ., Bangkok.
Nuntiyakul, W., P. Evenson, D. Ruffolo, A. Sáiz, J. W. Bieber, J. Clem, R. Pyle, M. L. Duldig, and J. E. Humble (2014), Latitude survey investigation of Galactic cosmic ray solar modulation during 1994–2007, *Astrophys. J.*, *795*, 11, doi:10.1088/0004-637X/795/1/11.
Picone, J. M., A. E. Hedin, D. P. Drob, and A. C. Aikin (2002), NRLMSISE-00 empirical model of the atmosphere: Statistical comparisons and scientific issues, *J. Geophys. Res.*, *107*(A12), 1468, doi:10.1029/2002JA009430.
Ruffolo, D., et al. (2016), Monitoring short-term cosmic ray spectral variations using neutron monitor time delay measurements, *Astrophys. J.*, *817*, 38, doi:10.3847/0004-637X/817/1/38.
Scherer, K., H. Fichtner, R. D. Strauss, S. E. S. Ferreira, M. S. Potgieter, and H.-J. Fahr (2011), On cosmic ray modulation beyond the heliopause: Where is the modulation boundary?, *Astrophys. J.*, *735*, 128, doi:10.1088/0004-637X/735/2/128.
Shibata, S., et al. (1997), Calibration of neutron monitor using an accelerator, in *Proceedings of the 25th International Cosmic Ray Conference*, vol. 1, Durban, South Africa.
Shibata, S., et al. (1999), Calibration of neutron monitor using accelerator neutron beam, in *Proceedings of the 26th International Cosmic Ray Conference*, vol. 7, p. 313, International Union of Pure and Applied Physics (IUPAP), Salt Lake City, Utah.
Shibata, S., et al. (2001), Detection efficiency of a neutron monitor calibrated by an accelerator neutron beam, *Nucl. Inst. Meth. Phys. Res.*, *A463*, 316–320, doi:10.1016/S0168-9002(01)00280-7.
Stone, E. C., A. C. Cummings, F. B. McDonald, B. C. Heikkila, N. Lal, and W. R. Webber (2013), Voyager 1 observes low-energy galactic cosmic rays in a region depleted of heliospheric ions, *Science*, *341*, 150–153, doi:10.1126/science.1236408.
Usoskin, I. G., K. Alanko-Huotari, G. A. Kovaltsov, and K. Mursula (2005), Heliospheric modulation of cosmic rays: Monthly reconstruction for 1951–2004, *J. Geophys. Res.*, *110*, A12108, doi:10.1029/2005JA011250.
Usoskin, I. G., A. Bazilevskaya, and G. A. Kovaltsov (2011), Solar modulation parameter for cosmic rays since 1936 reconstructed from ground-based neutron monitors and ionization chambers, *J. Geophys. Res.*, *116*, A02104, doi:10.1029/2010JA016105.
Zhang, M., X. Luo, and N. Pogorelov (2015), Where is the cosmic-ray modulation boundary of the heliosphere?, *Phys. Plasmas*, *22*, 91501, doi:10.1063/1.4928945.